Int J CARS (2007) 2:65–73
DOI 10.1007/s11548-007-0119-z

ORIGINAL ARTICLE

Accuracy evaluation of initialization-free registration for intraoperative 3D-navigation

Georgi Diakov · Wolfgang Freysinger

Received: 1 December 2006 / Accepted: 29 April 2007 / Published online: 29 June 2007

Abstract
Purpose An initialization-free approach for perioperative registration in functional endoscopic sinus surgery (FESS) is sought. The quality of surgical navigation relies on registration accuracy of preoperative images to the patient. Although landmark-based registration is fast, it is prone to human operator errors. This study evaluates the accuracy of two well-known methods for segmentation of the occipital bone from CT-images for use in surgical 3D-navigation.
Method The occipital bone was segmented for registration without pre-defined correspondences, with the iterative closest point algorithm (ICP). The thresholding plus marching cubes segmentation (TMCS), and the deformable model segmentation (DMS) were compared quantitatively by overlaying the areas of the segmentations in cross-sectional slices, and visually by displaying the pointwise distances between the segmentations in a three-dimensional distance map relative to an expert manual segmentation, taken as a "ground truth".
Results Excellent correspondence between the two methods was achieved; the results showed, however, that the TMCS is closer to the "ground truth". This is due to the sub-voxel accuracy of the marching cubes algorithm by definition, and the sensitivity of the DMS method to the choice of parameters. The DMS approach, as a gradient-based method, is insensitive to the thresholding initialization. For noisy images and soft tissue delineation a gradient-based method, like the deformable model, performs better. Both methods correspond within minute differences less than 4%.
Conclusion These results will allow further minimization of human interaction in the planning phase for intraoperative 3D-navigation, by allowing to automatically create surface patches for registration purposes, ultimately allowing to build an initialization-free, fully automatic registration procedure for navigated Ear-, Nose-, Throat- (ENT) surgery.

Keywords Marching cubes · Deformable models · Surgical navigation · ENT · FESS

G. Diakov (✉) · W. Freysinger
4D Visualization Laboratory, University Clinic of Oto-, Rhino-, Laryngology, Innsbruck Medical University, Anichstraße 35, 6020 Innsbruck, Austria
e-mail: georgi.diakov@i-med.ac.at

Introduction

Clinical applications for 3D-navigation in oto-, rhino-, laryngology ideally require sub-millimetric application accuracy, to avoid iatrogenic lesions of minute and delicate anatomic structures. In video-endoscopic functional endoscopic sinus surgery (FESS) these are e.g. the internal carotid arteries, the orbit, the anterior skull base and the brain. Navigated microscopic surgery has to meet even higher standards for "useful" application accuracy as the display of navigated structures in the oculars is extremely sensitive to tracking errors [1]. Landmark-based registration is fast, but requires user interaction for thresholding and the definition of anatomic landmarks for the physical registration process, which makes it prone to human errors. A segmentation-based registration allows for surface matching, without pre-defined correspondences (e.g. with the iterative closest point algorithm — ICP [2]). It relies on the accuracy of the segmentation, which determines its clinical application accuracy and success.

Medical images need to be segmented for a series of tasks: surgery planning, registration of the patient to the imagery (the physical registration process), diagnosis, visualization and teaching [3,4]. Segmentation needs to be verified against a figure of merit, established by statistical analysis of all possible variations in the segmentation. The segmentation

methods and the criteria for their evaluation differ, depending on the clinical application. So, volumetric and intensity-based approaches cannot be used for the patient-to-image registration process. Bone can easily be segmented with practically any of the known segmentation techniques [3,4]. Each clinical application, however, is tailored for specific anatomy and surgery, with specific radiologic imaging. Certainly, there are other advanced segmentation methods available like the level-sets method [5], which is a 4D-representation of the evolution of the surface along the series of slices [3,4]. The method evolves the surface by updating the level set function, which is an Eulerian formulation of motion which basically "moves" the segmented surface, so that it is cut by the slice plane at different levels. For standalone use, the level-sets method is quite a powerful tool in surface segmentation, but the drawback is the lack of convergence, when many concavities are present on the segmented surface [3]. Other commonly used segmentation methods — watershed [3] and adaptive thresholding [4], are available. However, the deformable model was chosen in order to specifically use a widely tested gradient-based approach suitable for use with osseous structures surrounded by "noisy" soft-tissues. For challenging clinical tasks various approaches exist and are combined to "segmentation frameworks" [4,6], where "simple" methods are applied in a sequence to achieve successful segmentation of anatomical structures in noisy datasets, with discontinuous surfaces and/or blurred boundaries [7]. We decided to use a rather simple method, deformable model segmentation [3,4], DMS, rather than exploring more advanced state-of-the-art approaches.

While grayvalue segmentation is widely implemented in modern navigation systems, model-based methods are still not in use for that clinical purpose, to the best of our knowledge. User interaction in the preparatory segmentation step of 3D-navigation is mostly based on a threshold grayvalue segmentation with the marching cubes algorithm [8] (TMCS) [9,10] to create a triangulated surface of the patient and a three-dimensional model of the patient, to select anatomical structures. Triangulations with the marching cubes algorithm are of sub-millimetric accuracy as the exact locations of the intersection points of the triangulated mesh are determined by linear interpolation of the grayvalues of the vertices of neighboring voxels. The literature describes various methods for the improvement of the definitions of the surface faces inside the voxels [11,12] and the optimization of the polygonization speed [13].

The other method under consideration in this work, the deformable model segmentation (DMS), uses this surface as input [3,4,6,8,14–17]. In DMS segmentation a gradient force-field [3], is calculated from the original grey-scale image to yield an optimized segmentation. The combination of these two methods is, apart of an irrelevant choice of a TMCS threshold (see later), the idea of initialization-free

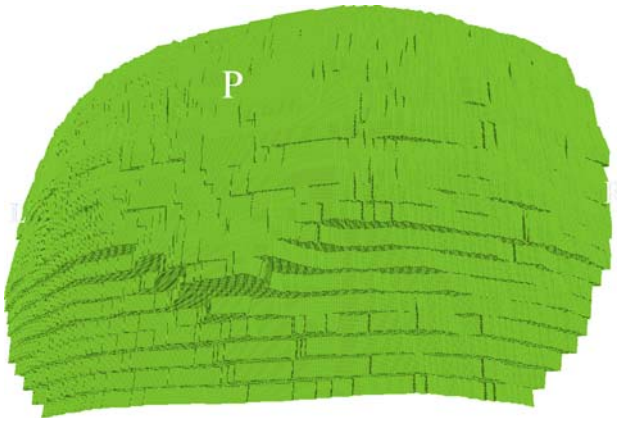

Fig. 1 The "ground truth" — an expert segmentation of the occipital bone in 3D-Slicer. The orientation is indicated as anterior (A) — posterior (P) and left (L) — right (R)

surface generation for registration for clinical 3D-navigation. As there is no "true" segmentation, some base for comparison is taken as "ground truth" to which the segmentations methods are compared through quantitative measurements [9,18]. The sharp contours of the bony skull in CT-images are a good basis for a quantitative evaluation of the segmentation methods under consideration here; we chose a manual expert segmentation as ground truth. This quantitative evaluation had to answer whether the DMS approach would yield results similar to the widely used TMCS implemented in clinical navigation systems.

Materials and Methods

A CT-dataset of the head with spatial resolution 0.39 × 0.39 × 2.5 mm and a sampling resolution of 512 × 512, acquired with a Siemens Somatom Plus 4 Volume Zoom scanner (Siemens, Erlangen, Germany) at the University Clinic of Radiology at the Medical University of Innsbruck was taken for the study. The "ground truth" (Fig. 1) was generated by averaging five manual segmentations in the 3D-Slicer [19] with MatLab [20]. Only voxels, that were contained in all five segmentations were included in the "ground truth". The posterior quarter of the CT-images, which contains all the anatomic features of interest, was taken for the segmentation of the occipital bone. Primarily to save computing time and to exploit the closed surface profile of this anatomic location. Moreover, for complete CT-slices leaking of region-growing through the natural openings of the bony skull inside would add structures to the segmentation and make the triangulation of a mesh for DMS impossible.

The TMCS-method is implemented in the VTK classes ImageThreshold and MarchingCubes, where the marching cubes algorithm is provided with a threshold value setting [21]. A region-growing algorithm [22] was applied after the threshold segmentation. It delineated the occipital surface as

a thin membrane, reducing the data in the segmentation to the structures of interest. Since in our clinical setting axial CT-slices are used that have the anterior direction in the upper part of the images we decided that the region-growing started from a seed in the posterior left corner of each slice in the image and grew, until it filled out the area, surrounded by the slice border (only of the posterior quarter) and the contour of the occipital bone. The resulting binary images were triangulated to yield the starting mesh for the DMS [22].

Basically there are two major types of formulations of DMS, the energy-minimization and the dynamic force formulation [22]. The deformable model implemented in the ITK class DeformableMesh3DFilter utilizes the latter one. While the energy-minimization deformable models minimize an energy function, whose solution satisfies a minimum principle to fit on the features of interest, the dynamic force formulated ones have the flexibility to apply different types of external forces onto the deformable surface. Both formulations of a minimization principle resemble the physical world that can be described by Lagrangian mechanics and the calculus of variations [23], providing the time-evolution of the deformable surface. In general, the dynamic force formulation has the form:

$$\mu \frac{\partial^2 X}{\partial t^2} = F_{\text{damp}}(X) + F_{\text{int}}(X) + F_{\text{ext}}(X) \tag{1}$$

which follows from Newton's second law. Here $X(t)$ is the parametric representation of the deformable surface, μ is a mass coefficient and $F_{\text{damp}}(X)$ is a damping (viscous) force, defined as $-\gamma\ \partial \text{X}/\partial \text{t}$ (γ is a damping coefficient). Since the deformable surface is accepted to have no mass characteristics, μ is set to zero. Then (1) becomes

$$\gamma \frac{\partial X}{\partial t} = F_{\text{int}}(X) + F_{\text{ext}}(X) \tag{2}$$

Equation (2) is the basis of the DMS method. (for detail, please see [6]). In summary, its dynamic formulation has the form:

$$\dot{d} + Kd = f_{\text{ext}} \tag{3}$$

Here $d(t)$ is the local deformation, $\dot{d} = \partial d/\partial t$, K is a stiffness matrix and f_{ext} is the gradient-derived external force. According to the theory of elasticity, the product Kd provides the forces of resistance of an elastic membrane, here associated with the internal forces that keep the mesh from disruption during deformation. The solution of (3) provides the time-dependent displacements for all nodes in the mesh, which is then updated with

$$d_{\text{new}} = \dot{d}\Delta t + d_{\text{old}} \tag{4}$$

where d_{new} and d_{old} are the new and the old position of a node respectively, $\dot{d} = \partial d/\partial t$, and Δt is the integration parameter.

The stiffness matrix has considerable influence on the deformation of the mesh. The choice of the parameters for its calculation is vital for tuning the deformable model. It is derived from the deformation strain energy, which in the theory of elasticity results from the integration of the stress and tensor vectors [4]. The stiffness matrix is

$$K = \int (\partial S)^T D \partial S\, du \tag{5}$$

Here S is the basis matrix, whose elements are basis functions, defining the geometry of the triangular elements in the mesh, ∂ is the differential operator, D is a symmetric matrix, derived from the local deformations, and u is the Cartesian coordinate. The basis matrix is 3×3, and its basis functions are the shape functions of a triangle. After the marching cubes triangulation, the deformable surface is discretized into triangular elements, and the shape functions are used to interpolate the displacement within an element. The differential operator ∂ is a 3×3 diagonal matrix with the elements $\partial/\partial u$, $\partial/\partial v$ and 1 along the main diagonal, where u and v are the Cartesian coordinates. The symmetric matrix D gives the relationship between the stress and the strain vectors (theory of elasticity). It is 3×3 with elements ω_{10}, ω_{01} and ω_{00} along the main diagonal, which are derived from the local deformations. The element ω_{00} controls the local magnitude of the deformation and ω_{10}, ω_{01} control the local variation of the deformation in the u, v directions, respectively. For simplicity, it is assumed that $\omega_{10} = \omega_{01} = \omega_1$ and $\omega_{00} = \omega_0$. The proper selection of ω_0 and ω_1 is decisive for the successful segmentation with the deformable model. Lower values of ω_0 and higher values of ω_1 make the mesh more resistant, which maintains its intactness, on the contrary higher ω_0 and lower ω_1 achieve better fit onto shapes of complex curvature.

The external force in (3) is derived from the image. It is formed by the second-order derivative gradient vector, according to

$$f_G(x, y, z) = -\vec{\nabla}\left(w_e \left|\vec{\nabla}[G_\sigma(x, y, z) * I(x, y, z)]\right|\right)^2 \tag{6}$$

Here $I(x, y, z)$ is the original image, w_e is a positive weighting parameter, $G_\sigma(x, y, z)$ is a 3D Gaussian function with standard deviation σ, $\vec{\nabla}$ is the gradient operator, and $*$ is the convolution operator. The image is blurred with a Gaussian filter to remove noisy regions and to expand the effective range of the gradient force. The absolute value of the force-vector at a node is calculated as the projection of the gradient-vector on the normal-vector at the node. The direction of the force vector is determined by the sign of this dot product by assigning positive signs to locations inside the surface and vice versa.

The stiffness matrix K is calculated for each node in the mesh. Then Eqs. (3) for all the nodes are solved with the finite elements method, and the mesh is evolved with (4).

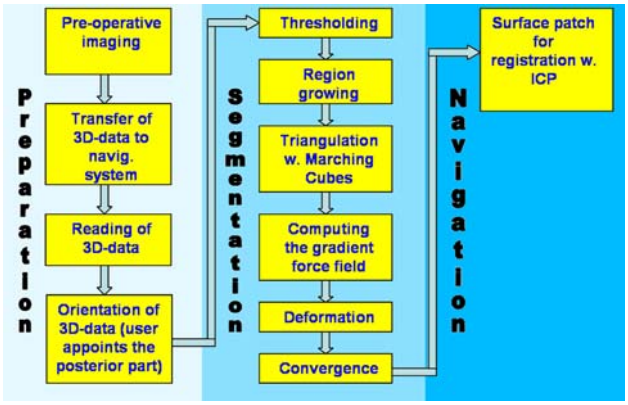

Fig. 2 Flowchart of the method, showing its integration in a potential clinical application

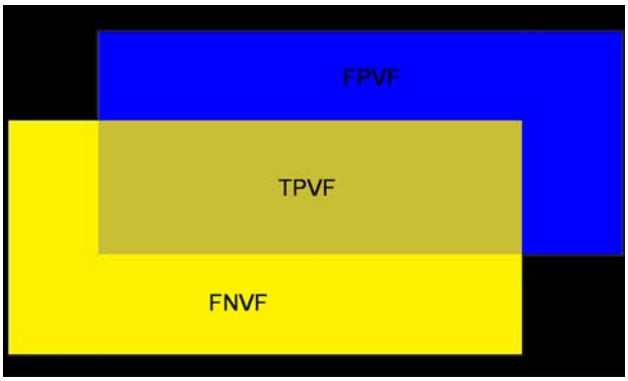

Fig. 3 Meanings of the three fractions, applied for the quantitative evaluation of the segmentations. This sketch graphically shows that the TPVF is that fraction of the "ground truth" segmentation that is correctly segmented by a certain method. Similar arguments hold for FPVF and FNVF; for abbreviations see text

The flowchart of the method (Fig. 2) shows the preparation and the sequence of the segmentation process.

The two segmentation methods were implemented with ITK, VTK and the fast light toolkit (FLTK) [24]. The dataset was segmented on a Pentium 4, 2.66 GHz PC with 256 RAM and GeForce FX 5200 graphics card, under Windows XP. The implementation in C++ is platform-independent and can be compiled for Linux, Mac OSX and Solaris. When the dataset is loaded, the operational parameters are set by the user and the steps of the automatic segmentation can be followed.

The accuracy of the two segmentations was evaluated in two ways. First, they were saved in slices as binary images and compared to the "ground truth". For each slice, three fractions were formed [18] (Fig. 3):

1. False Negative Volume Fraction (FNVF) — the area, contained in the "ground truth", while missed by the segmentation, divided by the area of the "ground truth".

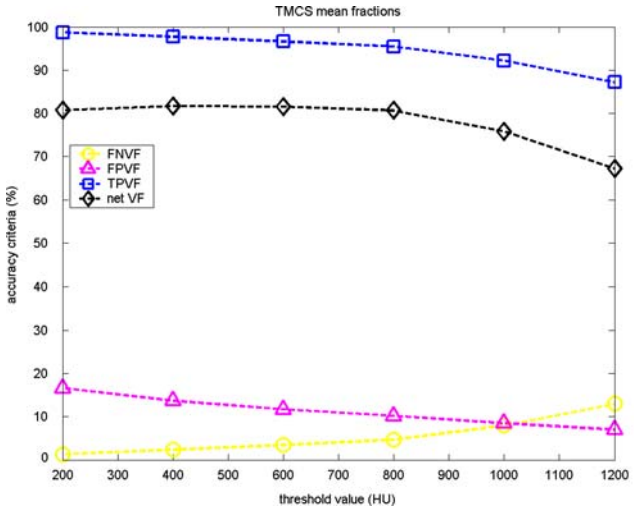

Fig. 4 Mean values of FNVF, FPVF and TPVF for TMCS with a threshold value in the interval [200, 1,200] HU, at steps of 200 HU

2. False Positive Volume Fraction (FPVF) — the erroneously segmented area, which is not contained in the "ground truth", divided by the area of the "ground truth".
3. True Positive Volume Fraction (TPVF) — the truly segmented area, divided by the area of the "ground truth".

A better segmentation is indicated by lower values of FNVF and FPVF, and higher values of TPVF, respectively. The image-arithmetic was conducted in MatLab [18]. A net volume fraction (net VF) was formed by subtracting the two false fractions (FNVF and FPVF) from the true fraction (TPVF) and taken for the quantitative estimation of the accuracy of the two segmentation methods.

The evaluation method was first used to determine the threshold value for TMCS (Fig. 4). The criteria compare the two segmentations at voxel-level [18]. Since model-based segmentations can extract shapes at sub-voxel level (the node-density in the mesh is higher than the density of the voxel grid) the CT-dataset was over-sampled by tripling the spatial resolution in z-direction. To apply the first accuracy evaluation method, the three-dimensional surfaces (meshes) of the two segmentations were intersected with the oversampled (tripled) CT-slices and each of them was compared slice-by-slice to the "ground truth", to achieve an accuracy estimation at sub-voxel level.

Second, the two segmentations were compared to each other in a pointwise manner and the distances between the pairs of corresponding points were presented in a distance-map graphic. The pointwise distance was calculated as the absolute Euclidean distance between the corresponding points in the two segmentations. Mathematically, the pointwise distance D_{pw} is:

$$D_{\mathrm{pw}} = \sqrt{(x_1 - x_2)^2 + (y_1 - y_2)^2 + (z_1 - z_2)^2} \qquad (7)$$

where x_1, y_1, z_1, x_2, y_2 and z_2 are the Cartesian coordinates of a node in the first and the second mesh, respectively.

Incorporating data accuracy in the visualization is a well-known approach, providing intuitive information about data quality, e.g. the uncertainty of the triangulation can be assigned to the hue values and displayed by rendering [25]. The pointwise distance has also been used to represent the variation of the segmented surface [6].

Results

The threshold value was set to 400 Hounsfield units (HU), to leave only bone in the image. The value was chosen after a comparison of TMCS to the ground truth for a series of threshold values (200, 400, 600, 800, 1,000, 1,200). As is well known, bone is displayed from 40 to 3000 HU in CT images. The graphical display of the results (Fig. 4) shows that all three criteria, i. e. FNVF, FPVF, and TPVF, respectively, vary slowly with the HU value over a broad range of HUs. While the FNVF and the TPVF show a better segmentation at 400 HU, these quality criteria deteriorate towards 1,200 HU; the FPVF value indicates a better segmentation at 1,200 HU than at 200 HU. The net VF was considered as a criterion for the choice of the threshold value. As can be seen from Fig. 4, the net VF is 81.7% at 400 HU, against 81.5 and 80.8% at 600 and 200 HU, respectively. For threshold values below 200 HU, the threshold-based segmentation failed.

While the TMCS is dependent on the initialization threshold value, even if this dependence varies slowly, the DMS is *independent* from the starting mesh and the thresholding HU value by construction, as long as the initial mesh is and its topology are "close" to the object to be segmented [6]. Figure 5 shows the three comparison criteria [18] and the net VF for the DMS segmentation. These parameters remain practically constant, with small variation for threshold values above 1,000 HU. This is due to the initial mesh as provided by the TMCS segmentation, see above.

The segmentation of the occipital bone in 3D-Slicer (the "ground truth") took up to one minute per slice, depending on the expertise of the observer. For the dataset used (25 slices), each manual segmentation took 15–25 min. The "ground truth" was generated from five manual segmentations, and the time needed could be estimated as 1.6 man-hours.

On the computer described, the TMCS method took 35 s, computing the gradient force field 40 s, and the deformation 7.4 s/iteration.

The deformation parameters were set to: $\Delta t = 0.01$ s, $\omega_0 = 0.14$, $\omega_1 = 0.05$. The most important parameter in Eq. (4) is Δt. Higher values of Δt increase the displacements at each iteration, this way the deformation requires less iterations to converge. The parameters ω_0 and ω_1 control the

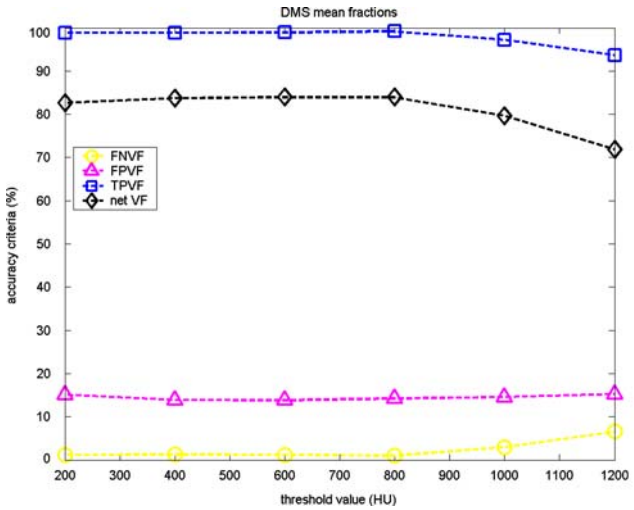

Fig. 5 Mean values FNVF, FPVF and TPVF for DMS with an initialization mesh, segmented with threshold values in the interval [200, 1,200] HU, at steps of 200 HU. The result is independent of the initialization

local magnitude and the local variation of the deformation, respectively [4,6]. Increasing ω_0 makes the mesh softer and more susceptible to fitting complex curvature on the shape. To maintain control on the deformation, higher values of ω_0 have to be applied together with lower values of ω_1. The settings of ω_0 and ω_1, 0.14 and 0.05, respectively, are for high degree of curvature in the shape [6]. They were chosen, in order to optimally imprint the feature of the lambda-fissure, ultimately needed for a successful patient-to-image registration with the ICP algorithm [4,6]. However, DMS is quite sensitive to the choice of parameters, but close correspondence between TMCS and DMS can be achieved with the proper parameter set best suited for the predominant curvature in the object.

The results from the comparison of TMCS and DMS to the ground truth with FNVF, FPVF and TPVF are presented in Figs. 6, 7, 8, and 9. Both methods agree closely, within a regime of less than 5%. The TMCS, Fig. 6, over the whole range investigated is closer to the "ground truth", with maximum differences $< 3\%$. The DMS, on the other hand, gives lightly worse results, with maximum differences to the ground truth $< 4\%$. All three criteria (FNVF, FPVF and TPVF) show a small, but systematically better adherence of the grayvalue segmentation to the "ground truth", see Figs. 6, 8 and 9. However, the differences are minute. The deformable model segmentation (yellow lines in all figures) shows predominantly higher FNVF and FPVF and lower TPVF values along the whole range of slices.

With deformation settings of ω_0 and ω_1, 0.07 and 0.1, respectively, the mesh is too stiff to fit the curvature of the shape, which leads to "springs" in the FNVF in areas with "bigger" steps between the adjacent slices (Figure 7). It can

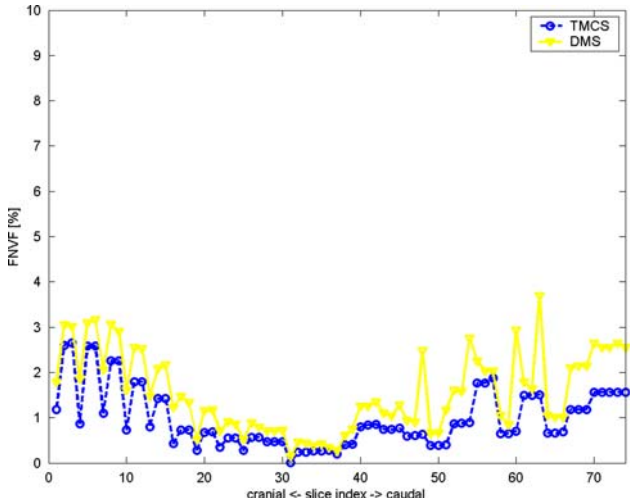

Fig. 6 False Negative Volume Fraction (FNVF) of the two segmentations. The TMCS systematically adheres better to the "ground truth"

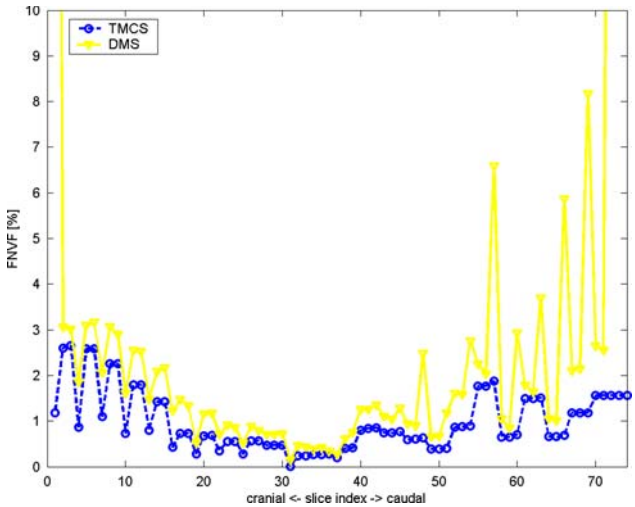

Fig. 7 False Negative Volume Fraction (FNVF) of the two segmentations with improperly set parameters of the deformation: $\omega_0 = 0.07$; $\omega_1 = 0.1$. The increased stiffness of the mesh has caused "springs" in the DMS segmentation in the areas with bigger "steps" between the slices

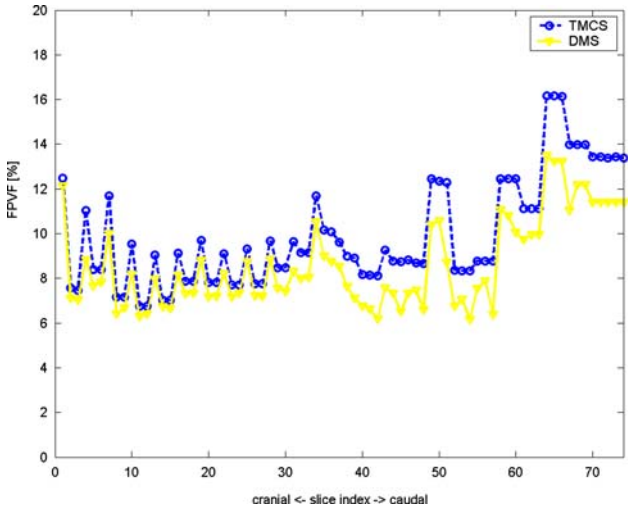

Fig. 8 False Positive Volume Fraction (FPVF) of the TMCS and DMS segmentations

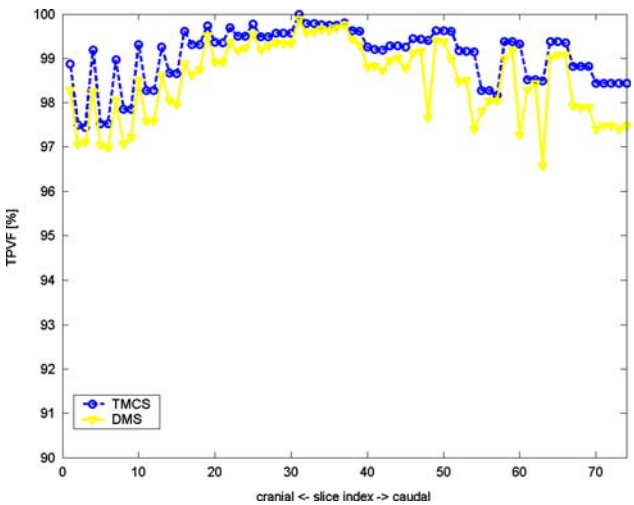

Fig. 9 True Positive Volume Fraction (TPVF) of the TMCS and DMS segmentations

be observed from the graphs, that for slice ranges with bigger "steps" in the shape between adjacent slices (see the encircled areas in Fig. 10), the TMCS method performs better, due to the implemented linear interpolation, the marching cubes algorithm does along the voxel edges. The two methods have practically identical adherence to the "ground truth" in slice ranges, with smaller "steps" of the contour between adjacent slices, see Figs. 6, 7, 8 and 9.

Figure 10 demonstrates the correspondence of the TMCS with "ground truth" segmentation. Both segmentations on the oversampled data set are triangulated to show the differences. For certain areas, as marked by the circles in the figure, a clear deviation is visible, as the inset of the area of the Lambda fissure shows. The graphical visualization of the DMS results as compared to the ground truth is seen in Fig. 11, for which a very similar behavior like with the TMCS can be noted, see the encircled areas and again the inset of the Lambda fissure.

As another evaluation criterion the pointwise distance measurement was used, where the two segmentations (TMCS and DMS) were compared to each other. Figure 12 shows the point-wise difference between the two segmentations as a color-coded distance map. The colors vary from light yellow to yellow, orange, red and dark red, corresponding to distances of below 0.2 mm, 0.2–0.4 mm, 0.4–0.6 mm, 0.6–0.8 mm and above 0.8 mm, respectively. This representation visualizes the progress of the deformation by coloring the areas, where the two segmentations differ. In areas with higher curvature, the differences grow, while the TMCS

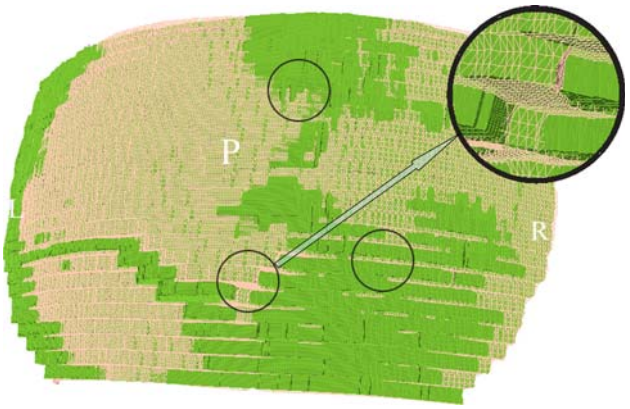

Fig. 10 A zoom in the mesh, displayed in 3D-Slicer. The oversampling is seen as three layers at each "step". The difference between the TMCS mesh and the "ground truth" is seen in the colored spots ("ground truth" *green*, TMCS *pink*). The three circles mark zones with visibly discernible differences in the segmentation; the inset is a magnification of one of these zones

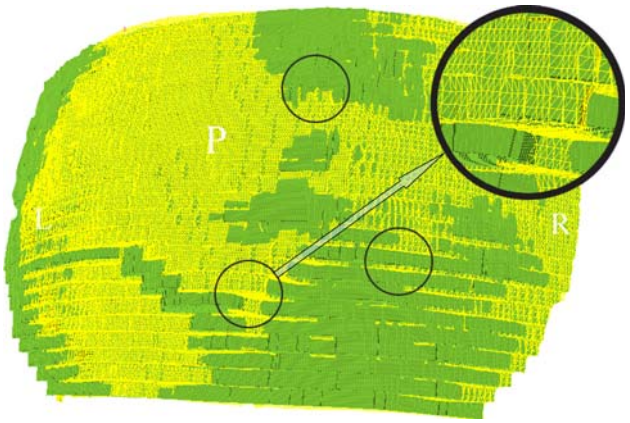

Fig. 11 A zoom in the mesh, displayed in 3D-Slicer. The oversampling is seen as three layers at each "step". The difference between the DMS mesh and the "ground truth" is seen in the colored spots ("ground truth" *green*, DMS *yellow*). Annotations as for Fig. 10

remains closer to the "ground truth". Note, however, that both methods (TMCS and DMS) correspond within a range $< 5\%$.

Figure 12 shows the deformation evolution of the mesh with these preset parameters at 120, 250 and 3,221 (convergence) iterations. The average pointwise distance was calculated by summing all values and dividing them by the number of points. The average, the maximal pointwise distance and the standard deviation are shown in Table 1.

The deformation iterates, either until it reaches the preset number of iterations, or converges. The number of iterations necessary is strongly dependent on the integration parameter Δt. Figure 13 shows how the number of iterations needed to reach convergence depend on the choice of Δt, 0.1 and 0.01 s, respectively. With higher values of Δt the deformation at each iteration is stronger and the algorithm converges much faster. Values of Δt above 0.1 s, however, lead to roughness

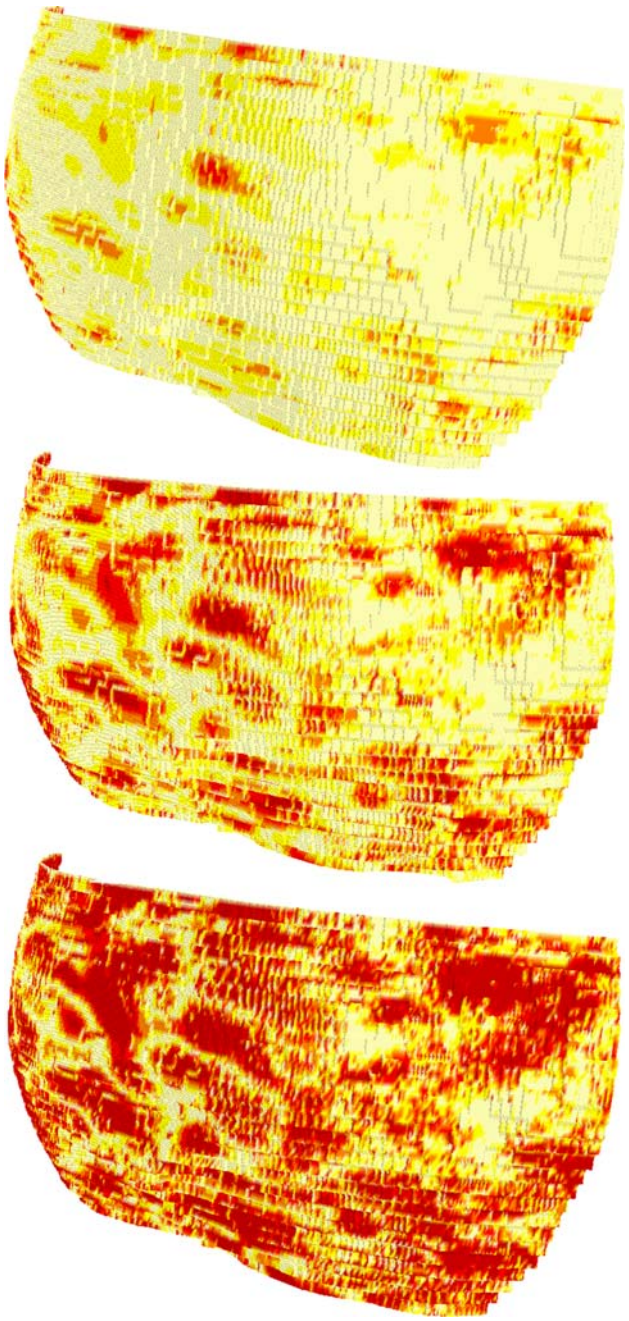

Fig. 12 A color-coded display of the pointwise distances of the deforming DMS mesh with respect to the initial TMCS mesh. Deformation parameters are: $\Delta t = 0.01$ s; $\omega_0 = 0.14$; $\omega_1 = 0.05$. The deformation progress is shown at 120, 250 and 3221 (convergence) iterations. The colors mean: *light yellow* distance below 0.2 mm, *yellow* 0.2–0.4 mm, *orange* 0.4–0.6 mm, *red* 0.6–0.8 mm and *dark red* above 0.8 mm

in the mesh, due to the intensity of local deformations. Lower values on the other hand lead to an impractically high number of iterations. This way the optimal range of Δt was established from 0.01 to 0.1 s ($\Delta t = 0.1$ s requires 317 iterations to converge, $\Delta t = 0.01$ s: 3,221 iterations, respectively).

Table 1 Deformation progress with fixed parameters (color-coded distance-map, Fig. 12)

No. of steps	Mean pointwise distance (mm)	Maximal pointwise distance (mm)	Standard deviation of the pointwise distance (mm)
120	0.0855	0.3	0.0725
250	0.332	0.625	0.1345
3221	0.3080	1.25	0.24

Deformation parameters are: $\Delta t = 0.01$ s; $\omega_0 = 0.14$; $\omega_1 = 0.05$

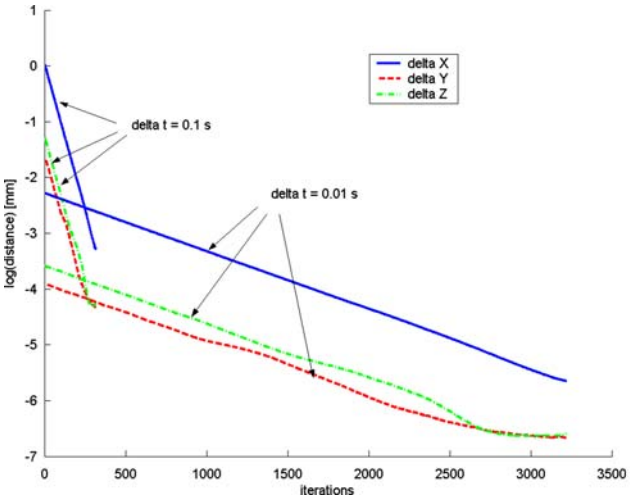

Fig. 13 Convergence behavior of the deformation process with $\Delta t = 0.1$ s and $\Delta t = 0.01$ s. Other deformation parameters are: $\omega_0 = 0.14$; $\omega_1 = 0.05$. The Y-axis shows the natural logarithm of the change in the coordinates $(\Delta x, \Delta y, \Delta z)$, calculated by the iteration, numbered on the X-axis

Discussion

Modern surgical 3D-navigation takes advantage of a variety of methods for registration and frameless stereotaxy. The inaccuracy of the registration accumulates along the sequence of operations, starting with the preoperative imaging. While the imaging modalities have reached a remarkable quality (spatial resolutions of below 0.4 mm), preoperative planning can still be improved with alternate segmentation methods and improving their clinical application.

The TMCS method applied the MarchingCubes class in VTK [21], which combines a grayvalue segmentation (thresholding) with a triangulation with the marching cubes algorithm. State-of-the-art navigation systems use this sequence for 3D-reconstruction, during the selection of landmarks for registration, to the best of our knowledge. However, they still do not make use of model-based segmentation methods, like DMS, which could improve the surface-based registration. In literature, deformable models are applied for fine-tuning of a TMCS of noisy data [3,6] (like in PET brain images [16] and in the segmentation of breast cancer [26]). Whether a further deformation of the segmented surface provides a better correspondence to reality much depends on the specificities of the clinical application - the signal-to-noise ratio (SNR) of the data, the accuracy requirements and the complexity of the segmented anatomy. While it could be expected, that on data with good SNR (like bone in CT-images) the TMCS performs better than DMS, the research of accuracy elements of both methods was oriented towards their mutual performance in a clinical application for surface-based registration for 3D-navigation.

Using the occipital bone for surface registration assures feature invariability. Since, mathematically, the registration under consideration is a rigid body transformation, the rigidity of the anatomy in the planning phase anatomy is a necessary predicament for a successful intraoperative registration. Skin shift is relevant if the facial relief or non-invasive markers are utilized for matching the patient to the preoperative radiologic data esp. in elderly patients and when muscle relaxing agents are applied intraoperatively [27]. However, use of select facial bone features (Nasion, Spina nasalis anterior, Sutura frontozygomatica) for patient-to-image registration purposes is potentially impaired due to the sterile draping of the patient. Additionally, “hidden” bony structures are not accessible directly [28]. ENT-surgery has become a minimally-invasive treatment, and using invasive markers and stereotactic frame fixation is generally not deemed acceptable. The occipital bone, as an alternative, provides the specific feature of the lambda-fissure for registration without predefined point correspondences with the ICP algorithm [28]. It can be accessed intraoperatively from below the operating table, without interference with the remaining setup in the operating room (OR) by e.g. ultrasound A-mode for intraoperative surface acquisition [29]. The described segmentation methods can be applied on the clinical routine CT-datasets for 3D-navigation in ENT-surgery. The principal goal of this study was to investigate the possibilities to use model-based segmentation methods for initialization-free segmentation and registration approaches in navigated ENT surgery. Such approaches are not implemented in the clinical navigation systems; instead, they widely use the TMCS method. While the TMCS is sufficient for a 3D-reconstruction of high-contrast objects in CT-imaging in the planning phase of a point-based registration (done with the 4-points algorithm [10]), the challenge for segmentation for navigational purposes lies in soft-tissue structures and MR imaging with the ICP algorithm. Although the TMCS method provided slightly better results for bone segmentation from CT-images, the gradient-based segmentation approach and its use in complementing the TMCS method can be potentially useful for automating the planning and registration steps of navigated interventions. Thus the initialization of intraoperative 3D-navigation will not rely on human interaction, which would make it less error-prone.

There are studies in literature [3,6], which apply deformable models to segment a closed surface of an entire organ or a complete region in the medical image, either starting from an initial estimation of the surface, or from a seed which is grown to fill out the segmented region. The described method segments a patch, containing the anatomy of interest. It reduces the data, while leaving the feature for registration, which is beneficial to the surface-matching algorithm. In the literature, the reduction of data, before triangulating the surface, is used as a rendering optimization [30], where only the visible part of the surface is triangulated for faster visualization. In the presented method, only the feature for registration is triangulated. While it is a common approach to use region-growing algorithms as an initialization for a deformable model [30], here the region-growing was applied as an intermediate step between TMCS and DMS, to localize the patch at the occipital bone, without user interaction.

The accuracy elements of TMCS and DMS were researched with validated quantification approaches [30], for the optimization of the segmentation step, and towards the clinical application of these methods for 3D-navigation in ENT-surgery.

Acknowledgements This study was partially supported by grant No. 9318 of the Jubilee Funds of the Austrian National Bank. Special thanks to Prof. Rainer Schubert, MD, from the University for Health Sciences, Medical Informatics and Technology (UMIT), Hall in Tyrol, Austria, for his support with knowledge and experience.

References

1. Wagner A, Schicho K, Birkfellner W, Figl M, Seemann R, Konig F, Kainberger F, Ewers R (2002) Quantitative analysis of factors affecting intraoperative precision and stability of optoelectronic and electromagnetic tracking systems. Med Phys 29(5):905–912
2. Besl PJ, Mckay ND (1992) A Method for Registration of 3-D Shapes. IEEE Trans. Pattern Anal Mach Intell 14(2):239–256
3. Sonka M, Fitzpatrick JM (2004) Handbook of medical imaging. SPIE. ISBN 0-8194-3622-4
4. Yoo TS (2004) Insight into images: principles for segmentation, Registration, and image analysis. AK Peters Ltd. ISBN 1-56881-217-5
5. Fritscher KD, Schubert R (2006) 3D image segmentation by using statistical deformation models and level sets. Int J CARS (1):123–135
6. Chen T, Metaxas D (2005) A hybrid framework for 3D medical image segmentation. Med Image Anal 9(6):547–565
7. Ferrari RJ (2004) Identification of the breast boundary in mammograms using active contour models. Med Biol Eng Comput 42(2):201–208
8. Cootes TF, Taylor CJ (1995) Active shape models — their training and Application. Comput Vision Image Understand 61(1):38–59
9. Lorensen WE, Cline HE (1987) Marching cubes: a high resolution 3d surface construction algorithm. Computer Graphics 21(4):163–169
10. Gunkel AR, Freysinger W, Thumfart WF (2000) Computer-aided 3D-navigation systems. Survey and location determination (in German). HNO 48:75–90
11. Shu R, Zhou C (1995) Adaptive marching cubes. Visual Comput 11:202–217
12. Lopes A, Brodlie K (2003) Improving the robustness and accuracy of the marching cubes algorithm for isosurfacing. IEEE Trans Visualizat Comput Graphics 9(1):16–29
13. Ju T, Schaefer SD (2003) Convex contouring of volumetric data. Visual Comput 19(7–8):513–525
14. Thirion J-P (1998) Segmentation and registration of multimodal medical images: From theory, implementation and validation to a useful tool in clinical practice. http://www.medicalimagecomputing.com/tools/downloads.php?fileID=179
15. McInerney T, Terzopoulus D (1996) Deformable models in medical image analysis: a survey. Med Image Anal 1(2):91–108
16. Mykkanen J, Tohka J (2005) Automatic extraction of brain surface and mid-sagittal plane from PET images applying deformable models. Comput Methods Programs Biomed 79(1):1–17
17. Putter S, Laffargue F (2006) Computational mesh generation for vascular structures with deformable surfaces. Int J CARS 1:39–49
18. Udupa JK (2002) A methodology for evaluating image segmentation algorithms. Proc SPIE. http://bil.bme.columbia.edu
19. http://www.slicer.org
20. Ueberhuber C, Katzenbeisser S (2002) MatLab 6.5 Eine Einführung. Springer, Heidelberg. ISBN 3-211-83826-0
21. http://public.kitware.com/VTK
22. Ibanez L (2003) The ITK software guide. Kitware, Inc. ISBN 1-930934-10-6
23. Goldstein H (1981) Klassische Mechanik [Classical Mechanics]. Akademische Verlagsgesellschaft, ISBN 3-400-001-34-1
24. http://www.fltk.org
25. Rhodes PJ, Laramee RS (2003) Uncertainty visualization methods in isosurface rendering. Eurographics, Short Papers:83–88. http://citeseer.ist.psu.edu/rhodes03uncertainty.html
26. Madabhushi A, Metaxas D (2003) Combining low-, high-level and empirical domain knowledge for automated segmentation of ultrasonic breast lesions. IEEE Trans Med Imag 22(2):155–169
27. Malthan D, Ehrlich G, Stallkamp J, Dammann F, Schwaderer E, Maassen MM (2003) Automated registration of partially defective surfaces by local landmark identification. Comput Aided Surg 8(6):300–309
28. Lavallee S, Sautot P, Troccaz J, Cinquin P, Merloz P (1995) Computer-assisted spine surgery: a technique for accurate transpedicular screw fixation using CT data and a 3-D optical localizer. J Image Guid Surg 1(1):65–73
29. Diakov GM, Freysinger W (2007) Intraoperative A-mode ultrasound for automatic registration in ENT 3D-navigation (a cadaver study). Poster presentation CARS, Berlin, Germany, 27–30 June 2007
30. Gao J, Shen HW (2003) Hardware-assisted view-dependent isosurface extraction using spherical partition. Joint EUROGRAPHICS — IEEE TCVG http://citeseer.ist.psu.edu/gao03hardwareassisted.html